Numerical simulation of liquid water and gas flow in a channel and a simplified gas diffusion layer model of polymer electrolyte membrane fuel cells using the lattice Boltzmann method

Yutaka Tabe [a,*], Yongju Lee [a], Takemi Chikahisa [a]
and Masaya Kozakai [b]

[a] Division of Energy and Environmental Systems, Graduate School of Engineering, Hokkaido University
N13 W8, Kita-ku, Sapporo 060-8628, Japan

[b] Department of Battery and Fuel Cell Systems, Hitachi Research Laboratory, Hitachi, Ltd., Japan
1-1, Omika-cho, 7-chome, Hitachi 319-1292, JAPAN

[*] Corresponding author. Tel.: +81 11 706 6381; fax: +81 11 706 7889.
E-mail address: tabe@eng.hokudai.ac.jp; N13 W8, Kita-ku, Sapporo 060-8628, Japan.

Abstract

Numerical simulations using the lattice Boltzmann method (LBM) are developed to elucidate the dynamic behavior of condensed water and gas flow in a polymer electrolyte membrane (PEM) fuel cell. Here, the calculation process of the LBM simulation is improved to extend the simulation to a porous medium like a gas diffusion layer (GDL), and a stable and reliable simulation of two-phase flow with large density differences in the porous medium is established. It is shown that dynamic capillary fingering can be simulated at low migration speeds of liquid water in a modified GDL, and the LBM simulation reported here, which considers the actual physical properties of the system, has significant advantages in evaluating phenomena affected by the interaction between liquid water and air flows. Two-phase flows with the interaction of the phases in the two-dimensional simulations are demonstrated. The simulation of water behavior in a gas flow channel with air flow and a simplified GDL shows that the wettability of the channel has a strong effect on the two-phase flow. The simulation of the porous separator also indicates the possibility of controlling two-phase distribution for better oxygen supply to the catalyst layer by gradient wettability design of the porous separator.

Keywords: PEM fuel cell, Lattice Boltzmann method, Two-phase flow, Large density difference, Gas diffusion layer, Wettability

Nomenclature

c : characteristic particle speed (m s^{-1})
$\boldsymbol{c}_i$: restricted velocities of particle ensembles (m s^{-1})
f_i : particle velocity distribution functions for the calculation of an order parameter
g_i : particle velocity distribution functions for the calculation of a predicted velocity
g : gravitational acceleration (m s^{-2})
H : vertical length of simulation domain (m)
L : characteristic length (m)

p : pressure (Pa)
Sh : Strouhal number
t : time (s)
t_0 : characteristic time scale (s)
Δt : time step during which the particles travel across the lattice space (s)
U : characteristic flow speed (m s^{-1})
$\boldsymbol{u}$: current velocity (m s^{-1})
$\boldsymbol{u}^*$: predicted velocity (m s^{-1})
x, y : position coordinates (m)
Δx : spacing of the cubic lattice (m)
κ_f : constant determining the width of the interface of two phases
κ_g : constant determining the strength of the surface tension
μ : viscosity (Pa s)
ξ : coordinate perpendicular to the interface (m)
ρ : density (kg m^{-3})
ρ_0 : reference density (kg m^{-3})
σ : interface tension (N m^{-1})
τ_f, τ_g : dimensionless single relaxation time
ϕ : order parameter
ϕ_0 : reference order parameter
superscript, subscript
eq : equilibrium state
in : inflow
G : gas
L : liquid
S : solid
α, β : Cartesian coordinates

1. Introduction

Water management is essential to improve the performance of polymer electrolyte membrane (PEM) fuel cells. While the membrane needs to be fully hydrated to maintain high proton conductivity, excessive amounts of water condense in the gas diffusion layers and gas flow channels and prevent the supply of reactants to the electrodes under high current density conditions. This phenomenon causes mass transport limitations and deteriorates the cell performance. The objective of this paper is to evaluate the dynamic behavior of condensed water and gas flows in a PEM fuel cell using numerical simulations, and an advanced lattice Boltzmann method for two-phase flow with large density differences was developed.

Understanding liquid water behavior in PEM fuel cells is of considerable practical significance. Several studies have been conducted on two-phase flows in PEM fuel cells. Theoretical one-dimensional models for liquid water transport in gas diffusion layers (GDLs), where liquid water is controlled by capillary forces depending on the structure and wettability of GDL, have been reported [1,2], and three-dimensional simulations using two-phase models have been developed [3,4]. For liquid water transport in gas flow channels, experimental investigations have been conducted using transparent fuel cells and it was demonstrated that the surface tension of water and the wettability of the GDL and gas flow channel play a

dominant role in the liquid water transport [5,6]. Some numerical simulations of the dynamic behavior of condensed water, which would be strongly affected by the wettability of GDL and gas flow channel, have been reported. The lattice Boltzmann method (LBM) was applied and it was established that LBM can be a powerful tool to estimate two-phase flow in the gas flow channels [7,8]. Two-dimensional simulation employing the volume of fluid (VOF) method were performed to investigate the dynamic behavior of a water droplet subjected to air flow in the bulk of the gas channel [9]. Recently, some simulations of condensed water distributions in a GDL have been developed using pore-scale modes, e.g. pore-network modeling, representing a porous medium at the microscopic scale by a lattice of wide pores connected by narrower constrictions termed throats [10] and a full morphology model relying on decomposing digital images of the GDL with pore radius as the ordering parameter at a specified pressure during drainage [11].

This paper develops the numerical simulation using the lattice Boltzmann method (LBM) to understand the dynamic behavior of condensed water and gas flow in a GDL and a gas flow channel. The LBM with the simple algorithm has a number of advantages as stated below, but is attended with much difficulty in maintaining continuity at the interface to simulate two-phase flows with large density differences like condensed water and air in a fuel cell. Here, the calculation process of the simulation was improved to extend the simulation in a porous medium like a GDL, and stable and reliable simulation of two-phase flows with large density differences in the porous medium was established. Using the improved simulation, the applicability of the LBM and appropriate conditions to simulate liquid water behavior in the GDL are discussed, and the significant advantages of this simulation, which can evaluate actual physical properties, were identified. Further, two-dimensional simulations demonstrated examples of the two-phase flow affected by the interaction between liquid water and air flows in a fuel cell. The effect of the wettability of the gas flow channel on the two-phase flow behavior was investigated, and the possibility of controlling the two-phase distribution using a porous separator without channels is presented.

2. Method of simulation

The LBM simulates mass and heat transport phenomena by tracking movements of particle ensembles where the velocities are restricted by a finite set of vectors. The particle population is expressed by distribution functions, and the time evolution of the distribution functions is calculated by a simple law of collision and transition, and it is shown that macroscopically the LBM is equivalent to a continuity equation and the Navier-Stokes equations for incompressible fluids. Additionally, introducing the interaction of the particles in the equation makes it possible to simulate multi-phase flow. Because of the simple algorithm, the LBM has a number of advantages: flexibility for complex boundary geometries, simplicity for parallel computing and accurate mass conservation. In multi-phase flow, tracking interfaces is not needed and distinct interfaces are maintainable without any artificial treatments. To simulate condensed water behavior in the 3-dimensional gas flow channels of a PEM fuel cell, the advanced LBM proposed by Inamuro *et al.* [12] was applied and the authors have confirmed that two-phase flows with large density differences, density ratios up to 1,000, can be calculated [7,8]. The greatest advantage of this LBM is that it can evaluate the

interaction between the gas flow and condensed water in the fuel cell where all the properties and conditions such as densities, viscosities, an interface tension, wettability and flow velocities can be simulated.

In the model, the non-dimensional variables are defined by a characteristic length L, a characteristic particle speed c, a characteristic time scale $t_0 = L/U$, where U is a characteristic flow speed, a reference order parameter ϕ_0, and a reference density ρ_0 is also used [12], and "non-dimensional" is represented by a circumflex. This paper uses a two-dimensional 9 velocities model (2D9V model) and the velocities of particle ensembles are restricted to the following vectors $\hat{\boldsymbol{c}}_i$ ($i = 1, 2, \ldots, 9$) in the 2-dimensional case as shown in Fig. 1 [13].

$$[\hat{\boldsymbol{c}}_1, \hat{\boldsymbol{c}}_2, \hat{\boldsymbol{c}}_3, \hat{\boldsymbol{c}}_4, \hat{\boldsymbol{c}}_5, \hat{\boldsymbol{c}}_6, \hat{\boldsymbol{c}}_7, \hat{\boldsymbol{c}}_8, \hat{\boldsymbol{c}}_9] = \begin{bmatrix} 0 & 1 & 0 & -1 & 0 & 1 & -1 & -1 & 1 \\ 0 & 0 & 1 & 0 & -1 & 1 & 1 & -1 & -1 \end{bmatrix} \tag{1}$$

Two particle velocity distribution functions, $\hat{f}_i$ and $\hat{g}_i$, are used. The $\hat{f}_i$ function is used for the calculation of an order parameter $\hat{\phi}$ which distinguishes two phases: $\hat{\phi} < \hat{\phi}_G$ corresponds to gas phase, $\hat{\phi} > \hat{\phi}_L$ liquid phase, and $\hat{\phi}_G \le \hat{\phi} \le \hat{\phi}_L$ the interface. The $\hat{g}_i$ function is used for the calculation of a predicted velocity of the two-phase fluid without a pressure gradient. The evolution of the particle distribution functions $\hat{f}_i$ and $\hat{g}_i$ with velocity $\hat{\boldsymbol{c}}_i$ at point $\hat{x}$ and time $\hat{t}$ are computed by the following equations.

$$\hat{f}_i(\hat{\mathbf{x}} + \hat{\boldsymbol{c}}_i \Delta\hat{t}, \hat{t} + \Delta\hat{t}) = \hat{f}_i(\hat{\mathbf{x}}, \hat{t}) - \frac{1}{\tau_f}[\hat{f}_i(\hat{\mathbf{x}}, \hat{t}) - \hat{f}_i^{eq}(\hat{\mathbf{x}}, \hat{t})] \tag{2}$$

$$\begin{aligned} \hat{g}_i(\hat{\mathbf{x}} + \hat{\boldsymbol{c}}_i \Delta\hat{t}, \hat{t} + \Delta\hat{t}) &= \hat{g}_i(\hat{\mathbf{x}}, \hat{t}) - \frac{1}{\tau_g}[\hat{g}_i(\hat{\mathbf{x}}, \hat{t}) - \hat{g}_i^{eq}(\hat{\mathbf{x}}, \hat{t})] \\ &+ 3E_i\hat{c}_{i\alpha}\frac{1}{\hat{\rho}}\left[\frac{\partial}{\partial\hat{x}_\beta}\left\{\hat{\mu}\left(\frac{\partial\hat{u}_\beta}{\partial\hat{x}_\alpha} + \frac{\partial\hat{u}_\alpha}{\partial\hat{x}_\beta}\right)\right\}\right]\Delta\hat{x} - 3E_i\hat{c}_{iy}\left(1 - \frac{\hat{\rho}_G}{\hat{\rho}}\right)\hat{g}\Delta\hat{x} \end{aligned} \tag{3}$$

Here, $\hat{f}_i^{eq}$ and $\hat{g}_i^{eq}$ are the equilibrium distribution functions, τ_f and τ_g are dimensionless single relaxation times, E_i is the associated weight coefficients presented below, $\Delta\hat{x}$ is the spacing of the cubic lattice, $\Delta\hat{t}$ is the time step during which the particles travel across the distance of the lattice spacing, $\hat{\rho}$ is the density, $\hat{\mu}$ is the viscosity, $\hat{\boldsymbol{u}}$ is the current

velocity and $\hat{g}$ is the gravitational acceleration. The subscripts α and β ($=\hat{x}, \hat{y}$) represent Cartesian coordinates and the summation convention is used. The third and last terms on the right hand side of Eq. (3) represent the effects of viscous stress and gravitation, respectively.

The order parameter $\hat{\phi}$ distinguishing two phases and the predicted velocity $\hat{\boldsymbol{u}}^*$ of the multi-component fluids are defined in terms of the two particle velocity distribution functions.

$$\hat{\phi} = \sum_{i=1}^{9} \hat{f}_i \tag{4}$$

$$\hat{\boldsymbol{u}}^* = \sum_{i=1}^{9} \hat{\boldsymbol{c}}_i \hat{g}_i \tag{5}$$

The equilibrium distribution functions $\hat{f}_i^{eq}$ and $\hat{g}_i^{eq}$ in Eqs. (2) and (3) are given by the following equations.

$$\hat{f}_i^{eq} = H_i\hat{\phi} + F_i\left[\hat{p}_0 - \kappa_f\hat{\phi}\frac{\partial^2\hat{\phi}}{\partial\hat{x}_\alpha^2} - \frac{\kappa_f}{6}\left(\frac{\partial\hat{\phi}}{\partial\hat{x}_\alpha}\right)^2\right] + 3E_i\hat{\phi}\hat{c}_{i\alpha}\hat{u}_\alpha + E_i\kappa_f G_{\alpha\beta}(\hat{\phi})\hat{c}_{i\alpha}\hat{c}_{i\beta} \tag{6}$$

$$\hat{g}_i^{eq} = E_i\left[1 + 3\hat{c}_{i\alpha}\hat{u}_\alpha - \frac{3}{2}\hat{u}_\alpha\hat{u}_\alpha + \frac{9}{2}\hat{c}_{i\alpha}\hat{c}_{i\beta}\hat{u}_\alpha\hat{u}_\beta + \frac{3}{2}\left(\tau_g - \frac{1}{2}\right)\Delta\hat{x}\left(\frac{\partial\hat{u}_\beta}{\partial\hat{x}_\alpha} + \frac{\partial\hat{u}_\alpha}{\partial\hat{x}_\beta}\right)\hat{c}_{i\alpha}\hat{c}_{i\beta}\right]$$

$$+ E_i\frac{\kappa_g}{\hat{\rho}}G_{\alpha\beta}(\hat{\rho})\hat{c}_{i\alpha}\hat{c}_{i\beta} - \frac{2}{3}F_i\frac{\kappa_g}{\hat{\rho}}\left|\nabla\hat{\rho}\right|^2 \tag{7}$$

Where,

$$E_1 = \frac{4}{9}, E_2 = E_3 = E_4 = E_5 = \frac{1}{9}, E_6 = E_7 = E_8 = E_9 = \frac{1}{36},$$

$$H_1 = 1, H_2 = H_3 = \cdots = H_9 = 0, F_1 = -\frac{5}{3}, F_i = 3E_i (i = 2,3,\cdots,9).$$

κ_f is a constant parameter determining the width of the interface between two phases, κ_g is a constant parameter determining the strength of the surface tension, and the parameters $\hat{p}_0$ and $G_{\alpha\beta}$ are explained in Ref. [7]. The interface tension $\hat{\sigma}$ is obtained by the following equation.

$$\hat{\sigma} = \kappa_g\int_{-\infty}^{\infty}\left(\frac{\partial\hat{\rho}}{\partial\hat{\xi}}\right)^2 d\hat{\xi} \tag{8}$$

Here, $\hat{\xi}$ is the coordinate perpendicular to the interface. The first and second derivatives are calculated using the LBM-specific finite-difference approximations [12].

Because the predicted velocity $\hat{\boldsymbol{u}}^*$ given by Eq. (5) is not satisfied by the continuity equation ($\nabla \cdot \hat{\boldsymbol{u}}^* = 0$), a correction of $\hat{\boldsymbol{u}}^*$ is required. The current velocity $\hat{\boldsymbol{u}}$ which satisfies the continuity equation can be obtained with the following equations.

$$Sh\frac{\hat{\boldsymbol{u}}-\hat{\boldsymbol{u}}*}{\Delta\hat{t}} = -\frac{\nabla\hat{p}}{\hat{\rho}} \tag{9}$$

$$\nabla\cdot\left(\frac{\nabla\hat{p}}{\hat{\rho}}\right) = Sh\frac{\nabla\cdot\hat{\boldsymbol{u}}*}{\Delta\hat{t}} \tag{10}$$

Here, $Sh = U/c$ is the Strouhal number and $\hat{p}$ is the pressure of the two-phase fluid; note that this definition gives the following relationships, $\Delta\hat{t} = Sh\Delta\hat{x}$, which is represented by $\Delta t = \Delta x/c$ with dimension and means that the particles travel across the lattice space Δx during time step Δt. This paper solved Eq. (10) using the successive over relaxation (SOR) method. Details of this model are described in a previous paper [7].

The scheme proposed by Seta and Takahashi [14] was applied to consider the wettability. In this scheme, the effect of wettability is established by the density of the solid wall. Since the intermolecular force is expressed in terms of density in the LBM, giving the density of a solid wall corresponds to giving the intermolecular force between liquid and solid wall. It was confirmed that this scheme can simulate the effect of wettability not only on a flat surface but also at a corner inside a gas flow channel [8].

3. Developments to the calculation process

The lattice Boltzmann method (LBM) for two-phase flow with large density differences has been applied to the simulation of liquid water and air flow in a PEM fuel cell [7] and the effect of wettability and cross-sectional shape on the liquid water behavior in the gas flow channels was reported [8] by the authors. However, there are problems with the reliability of simulated results in that there is nonconservation of the mass of the liquid water. Further, difficulties to simulate the two-phase flow in a porous medium such as in a modified gas diffusion layer (GDL) have been found. This study introduced some innovations to the calculation process and their effectiveness was confirmed. This paper presents an outline of explanations of the key improvements in the method of solving the Poisson equation (10) and

the settings of the boundary conditions for the pressure $\hat{p}$ on the wall and the particle distribution function $\hat{f}_i$ at the inlet.

Inamuro *et al.* solved the Poisson equation using an additional LBM [12], while here the equation is solved using the successive over relaxation (SOR) method as in the case of a conventional fluid simulation because of its easy implementation. The SOR is a commonly-used solution algorithm in conventional fluid simulations [15]. With the SOR it is possible to combine the LBM with conventional fluid simulation, but it is necessary to introduce a suitable grid transformation. In the LBM, co-location of a grid where velocity and pressure are defined at the same grid points, as shown in Fig. 2 (a), is used. In the SOR method, the calculation using the co-located grid induces spatial pressure oscillations. To prevent the spatial oscillation, the defined velocity grid points were transformed as shown in Fig. 2 (b), and the SOR method used this staggered grid. As the LBM treats the diagonal velocities the same as the orthogonal velocities, a formulation based on the grid in Fig. 2 (c) was also conducted.

The following will present an example of a 2-dimensional simulation for the change to the liquid water droplet in stationary air without gravity, to show the improvement that this causes. The domain is divided into 60 x 40 square cells in the $\hat{x}$ and $\hat{y}$ directions ($\Delta\hat{x}$ = 2.5 x 10^{-2}), and a liquid droplet with $5\Delta\hat{x}$ radius is placed at the center. The bottom and top of the domain are solid walls, and the left and right sides are given as free outflow conditions. The non-dimensional parameters for LBM are $\tau_f = 1$, $\tau_g = 1$, $\kappa_f = 0.5(\Delta\hat{x})^2$, $\hat{\phi}_L$ = 0.092 and $\hat{\phi}_G$ = 0.015, and the properties for the liquid water and the air are the same as in the next section. While the liquid water droplet gradually spread in the conventional simulation, the droplet in the improved simulation maintained its diameter practically unchanged. Fig. 3 shows a comparison between the conventional and the improved simulations of mass change of stationary liquid water droplets. It is confirmed that the mass conservation of the liquid water is clearly satisfied in the improved simulation.

In the extended calculation from flow in a gas channel to flow in a modified GDL, the continuity was still broken and inappropriate two-phase behavior was observed in some cases even with the improved method of solving the Poisson equation. This was caused by the boundary conditions for the pressure at the corner in the modified GDL as shown in Fig. 4 (a). The boundary condition for the pressure was set to keep the pressure gradient zero at the wall in solving the Poisson equation, and the pressure value on the wall was given by that at the neighboring cell on the fluid side. Similarly, the pressure at a corner like point *a* in Fig. 4 (a) was given as the equivalent of the average pressure at the adjacent fluid points *c* and *d*. This boundary condition sometimes induced non-negligible errors in the correction of the predicted velocity $\hat{\boldsymbol{u}}^*$ using Eq. (9). This study did not set the pressure at the corner to a certain value but adjusted it in each direction like (*a*-*b*) or (*a*-*c*) to make the pressure gradients zero. This means that point *a* has different pressure values to give a zero pressure gradient for each direction, which is a computational technique to prevent the non-negligible errors. It was

confirmed that this improvement of the boundary condition for the pressure results in good continuity in the modified GDL.

Another problem of simulation in the modified GDL was that the liquid flow rate from inlet boundary decreased when the liquid passed through the GDL. The particle distribution function $\hat{f}_i$ at the first grid at the inlet as shown in Fig. 4 (b) was set previous to be the equilibrium distribution function $\hat{f}_i^{eq}$ calculated by Eq. (6) using the inlet conditions, the order parameter $\hat{\phi}$ of the inlet fluid and the velocity $\hat{\boldsymbol{u}}$. However, in the case that the pressure drop in the inlet fluid increased, the order parameter $\hat{\phi}$ at the second grid in Fig 4 (b) was increased, and the reverse $\hat{f}_i$ values became larger. This induced the problem that the mass flow rate of the inlet fluid into the simulated domain decreased. In this study, the inlet particle distribution function $\hat{f}_i$ at the first grid is calculated to maintain a set flux $\hat{\phi}\hat{\boldsymbol{u}}$ between the first and second grids using the values of the second grid. This boundary condition for the particle distribution function $\hat{f}_i$ at the inlet makes it possible to control the inlet mass flow rate into the modified GDL accurately.

4. Results and Discussion

4.1. Liquid water behavior in a porous medium

Two-phase relatively slow flow in a porous medium is governed by capillary and viscous forces and different flow regimes are described by the relation of these forces [16]. The capillary number $Ca = u\mu_L/\sigma$, which represents the ratio of viscous to capillary forces, is an important parameter in the behavior of condensed water behavior in a GDL: for a typical fuel cell application, the capillary number Ca is of the order of 10^{-8}, and two-phase flow in a GDL falls in the regime of capillary fingering [10]. This section discusses the effects of capillary number Ca on the liquid water behavior in a porous medium using the LBM for the two-phase flow with large density differences, and also appropriate conditions to simulate the liquid water behavior in the porous medium of PEM fuel cells.

Fig. 5 shows two-dimensional simulations of liquid water flowing into a modified GDL with three different water velocities. The whole domain is divided into 100 x 50 square cells in the x and y directions. The vertical length of the simulated domain is H = 0.1 mm. The bottom, y = 0 mm, corresponds to a micro porous layer (MPL), and there are liquid water inflows with a velocity of u_L^{in} from the 20μm wide pore at the center of the MPL. The two sides, x = 0 and 0.2 mm are solid walls, and there is a free outflow opening at the top, y = 0.1 mm. Obstacles simulating the carbon fibers in a GDL are added, and the porosity of the porous medium is 0.8 with a maximum pore diameter of about 30 μm. The solid surfaces are

all set to hydrophobic with the contact angle of 150°, with the order parameters $\hat{\phi}_S$ 0.025. The simulated GDL properties, the porosity, the maximum pore diameter and the contact angle, are within the typical range of the actual GDLs. The GDL in this calculation can be a first stage model of an example of modified GDLs in the 2-dimensional simulation. All the properties of liquid water and air are the actual established values. The density ratio of the liquid water to the air is ρ_L/ρ_G = 847 (ρ_L = 997 kg m^{-3}, ρ_G = 1.18 kg m^{-3}), the viscosities of the water and air are μ_L = 8.54 x 10^{-4} Pa s and μ_G = 1.86 x 10^{-5} Pa s, and the interfacial tension between water and air is σ = 7.29 x 10^{-2} N m^{-1}. The time step Δt is set to 1.0 x 10^{-9} s and the gravitational acceleration is g = 0 m s^{-2}. The other non-dimensional parameters for LBM are the same as in the previous section. The finer time step and grid size ensure better convergence and accuracy of the simulation basically, but they induce longer computation time. The appropriate time step and grid size were selected by analyzing their effects on the simulation of the liquid water and the gas flow in a channel and a simplified GDL. Fig. 5 (a) shows the simulation results with the fastest inlet velocity of liquid water u_L^{in} = 2.0 m s^{-1}, and the capillary number Ca = 2.3 x 10^{-2}. After filling the first pore, the liquid water progresses through all four throats (left in Fig. 5 (a)). Then, it spreads out to both sides and grows into an almost homogeneous liquid phase from the bottom (right in Fig. 5 (a)). In Fig. 5 (b), where the inlet velocity is u_L^{in} = 0.20 m s^{-1} and the capillary number Ca = 2.3 x 10^{-3}, the liquid water flows selectively into relatively-wide throats and pores and the direction of progress is limited to two paths (Fig. 5 (b)). With the slowest velocity u_L^{in} = 0.020 m s^{-1} and the smallest capillary number Ca = 2.3 x 10^{-4} in Fig. 5 (c), liquid water also progresses into two throats in the early-stages (left in Fig. 5 (c)). However, once the largest path has grown diagonally upward left, the liquid water in the other, right, throat recedes and flows into the main branch: finally only one path, the one through the largest throats and pores is developed (right in Fig. 5 (c)). This phenomenon of receding water in a GDL is discussed in the next section.

These simulation results show that the selectivity of liquid water progression in a GDL increases with decreasing capillary number. This is because the effect of the capillary force on water behavior becomes dominant over the viscous force. Although the capillary number in the simulation is much larger than that in a typical fuel cell application where Ca is of order of 10^{-8}, the results in Fig. 5 (c) simulate the capillary fingering well, and is considered to be close to the actual behavior of liquid water in a GDL. Because it requires huge amounts of computation time to simulate the extremely slow production of the liquid water in the actual fuel cell, the following simulations use 0.02 m s^{-1} as the inlet velocity of the liquid water to shorten computation time.

Similar simulations were conducted, with the vertical length of the simulated domain H changed from 0.1 mm to 1.0 mm, and the time step Δt 1.0 x 10^{-8} s. Here, the maximum pore diameter becomes about 0.3 mm and this simulates liquid water behavior in a porous separator without channels, like that recently proposed as an alternative to cells with gas flow channels [17,18]. The results in Figs. 6 (a), (b) and (c) correspond to those at right in Fig. 5. In spite of the 10 times domain height H, the liquid water distributions are very similar. These simulation results indicate that two-phase flows in the porous medium with the same capillary number are analogous in the range of relatively-slow velocities because the length effects on the capillary and viscous forces cancel out.

The LBM simulation, considering capillary, viscous and inertial forces, confirmed that it is possible to simulate the similarity of capillary number *Ca* in two-phase flows in PEM fuel cells. Further, the LBM in this study, which considers actual physical properties, offers significant advantages in evaluating two-phase phenomena affected by the interaction between liquid water and air flows.

4.2. Effect of air flow in gas flow channel on the liquid water behavior

The simulation of liquid water behavior in a GDL with air flow in the gas flow channel was conducted as an example of a two-phase flow affected by the interaction between liquid water and air flows in fuel cells. Fig. 7 shows a schematic diagram of the computation domain: the whole domain is divided into 100 x 35 square cells in the x and y directions; the vertical length of the simulation domain is H = 1.0 mm; the upper and the lower parts correspond to a gas flow channel and a simplified GDL where the channel height is set relatively shallow to investigate effects of the upper separator wall on the liquid water because the drag force of air on liquid water becomes much stronger in a two-dimensional channel than in an actual three-dimensional channel. The uniform air flow and free outflow condition are at the left inlet side, x = 0 mm, and at the right outlet side, x = 2.9 mm, except in the bottom parts. Uniform flows of liquid water are also given at the bottom, y = 0 mm. The velocities of inlet air and liquid water are 0.05 m s^{-1} and 0.02 m s^{-1}. The obstacles simulating the simplified GDL are hydrophobic with the contact angle of 150° (the order parameter $\hat{\phi}_S$ = 0.025) and the effect of the wettability of the separator is examined using hydrophobic (contact angle 150°, $\hat{\phi}_S$ = 0.025) or hydrophilic (contact angle 40°, $\hat{\phi}_S$ = 0.080) walls; Δt is 1.43 x 10^{-7} s, and the properties of liquid water and air, and the other parameters for the LBM are the same as in the calculations above.

Fig. 8 shows the simulation results with the hydrophobic separator wall. The liquid water progresses selectively through the wider pores, as in Fig. 8 (a). When the liquid water exits to the channel, the liquid water body is broken up and the adjacent water branch in the narrow GDL pore recedes, Fig. 8 (a), (b). This phenomenon has been suggested from ex situ visualization of liquid water in a GDL using fluorescence microscopy [19], and shows that the LBM can simulate this phenomenon. After exiting to the channel, the liquid water forms into a droplet and is drained by the air flow in the channel (Fig. 8 (b)). Fig. 9 shows the results with the hydrophilic separator wall. The liquid water expelled from the GDL is attracted by the hydrophilic separator and forms a water film along the wall (Fig. 9 (a), (b)). This attracting of the water produces a void space and air flow near the interface between GDL and channel (Fig. 9 (b)). This may be expected to improve the flooding characteristics.

The simulation results confirm that the LBM is effective to simulate two-phase flows affected by the interaction between liquid water and air flows, and suggests that the wettability of the gas flow channel is important for the two-phase flow in a fuel cell. It further suggests that control of the wettability of the separator can result in a favorable distribution of liquid water and air flows.

4.3. Liquid water and air flow behavior in a porous separator without channels

To ensure a favorable distribution of liquid water and reliable air flow, a cell with a porous separator without channels was simulated. The porous separator has recently been proposed as an alternative to cells with gas flow channels, and the structure without channels is expected to enable a realization of uniform reaction over the active area of the membrane electrode assembly [17,18]. Fig. 10 shows a schematic diagram of the computation domain: the obstacles simulating the porous separator and the pore on the bottom MPL in Fig. 6 are to the left, and some further arrangements were added. The whole domain is divided into 100 x 50 square cells in the x and y directions. The vertical length of the simulated domain is H = 1.0 mm. The top is a wall, and uniform air flow and the free outflow are provided at the left inlet side, x = 0 mm, and at the right outlet side, x = 0.2 mm. A uniform flow of liquid water is also provided at the bottom pore of MPL, the velocities of inlet air and liquid water are 0.05 m s^{-1} and 0.02 m s^{-1}. To discuss the water and air flow distributions in the porous separator, the domain is divided into three regions, (I) lower, (II) intermediate, and (III) upper, as shown in Fig. 10. Two cases with different wettabilities of the porous separator were simulated; the solid surfaces were all hydrophobic (contact angle 150°, $\hat{\phi}_S$ = 0.025) and the upper shaded portions are changed to hydrophilic (contact angle 40°, $\hat{\phi}_S$ = 0.080); Δt is 1.0 x 10^{-7} s, and the properties of liquid water and air, and other parameters for the LBM are same as the calculations above.

Fig. 11 shows the changes in water weight and average air flow rates along the separator for each region in the hydrophobic porous separator. Before 0.100 s, the liquid water weight in region I increase first followed by increases in region II, as shown in Fig. 11 (a). Simultaneously, the average air flow rates in regions I and II decrease, increasing the air flow rate in region III, Fig. 11 (b), where the initial air flow rates at the 0 s in each region are very similar. Fig. 12 shows the appearances of the areas of liquid water (black) and air flow (uncolored) in the hydrophobic porous separator at three time points. Different from Fig. 6 (c), the liquid water does not move diagonally upward left, but due to the effect of air flow it moves through the right throat (Fig. 12 (a)). Then, liquid water proceeding upward is broken up and drained by the strong air flow in region III, establishing a dynamic equilibrium (Fig. 12 (b), (c)). Thus, the increase in the water weight in region III is suppressed and the oscillations in average air flow rates in Fig. 11 (b) after 0.150 s are caused by the breakup of the liquid water body.

Fig. 13 shows the changes in water weight and average air flow rates along the separator for each region in the hydrophobic-hydrophilic porous separator. (The upper shaded portions in Fig. 10 are here changed to hydrophilic.) Fig. 14 is the appearance of the area of liquid water (black) and air flow (uncolored) at three time points in the hydrophobic-hydrophilic porous separator. The liquid water weight grows in region III, attracted to the hydrophilic porous separator (Fig. 14 (a)). This induces the increase in water weight in region III after 0.106 s (Fig. 13 (a)), and the average air flow in region III decreases to nearly zero (Fig. 13 (b)), forming a liquid water region along the top wall (Fig. 14 (b)). In region II, the liquid water weight decreases and the average air flow rate increases drastically (Fig. 13 (a), (b)).

The liquid water is broken up by the strong air flow in region II, and a dynamic equilibrium is maintained after 0.240 s (Fig. 14 (b), (c)). It should be noted that the liquid phase along the top wall is drained by the air flow in region II continuously and maintained a certain amount, and the dynamic equilibrium can not be realized by replacing the liquid water phase with a solid wall in region III. This air path can be anticipated to contribute to better cell performance because reaction gas is easily supplied to the reaction area under the bottom. Overall, the simulation results show that controlling wettability of the porous separator is effective to realize an optimum two-phase distribution, where the air flow occurs between reaction area and condensed water.

5. Conclusions

The numerical simulations using the lattice Boltzmann method (LBM) for two-phase flows with large density differences has been developed to understand the dynamic behavior of condensed water and gas flows in a polymer electrolyte membrane (PEM) fuel cell. The calculation process of the LBM simulation, e.g. the discretization procedure in solving the Poisson equation and the boundary conditions for pressure at corners and the particle distribution function at the inlet, was improved to extend the application of the simulation in a porous medium like a gas diffusion layer (GDL). With the improvements a stable and reliable simulation of two-phase flows with large density differences in a porous medium was possible. Using the improved simulation, the applicability of the LBM and suitably selected conditions to simulate liquid water behavior in the GDL are discussed, and the significant advantages of this simulation, which can consider actual physical properties, are demonstrated. First, it is shown that dynamic capillary fingering can be simulated at lower migration speeds of liquid water in a modified GDL, and that the LBM simulation, considering capillary, viscous and inertial forces, simulates the similarity of capillary number, *Ca*, in two-phase flow in a PEM fuel cell. Then, as examples of the two-phase flow affected by the interaction between liquid water and air flows, two-dimensional simulations with air flow in a simplified GDL with a gas flow channel and in a porous separator are demonstrated. The simulation in the simplified GDL suggested that the wettability of the channel strongly influences the two-phase flow in a fuel cell, and the possibility that control of the wettability of the separator can be used to assist in an efficient distribution of liquid water and air flows. The simulation in the porous separator without channels also showed that controlling the wettability of the porous separator is more effective to realize an optimum two-phase distribution with the air flow formed between the reaction area and condensed water.

Acknowledgment

The authors thank Prof. Inamuro (Kyoto University) and Prof. Oshima (Hokkaido University) for helpful comments on the LBM scheme. We also thank Mr. K. Kibo (a master's student of Hokkaido University) for invaluable contribution to the development of the simulation.

References

[1] J. H. Nam, M. Kaviany, M., Int. J. Heat Mass Transfer 46 (2003) 4595-4611.
[2] U. Pasaogullari, C. Y. Wang, J. Electrochem. Soc. 151 (3) (2004) A399-A406.
[3] T. Berning, N. Djilali, J. Electrochem. Soc. 150 (12) (2003) A1589-A1598.
[4] G. Luo, H. Ju. C. Y. Wang, J. Electrochem. Soc. 154 (3) (2007) B316-B321.
[5] K. Tüber, D. Pócza, C. Hebling, J. Power Sources 124 (2003) 403-414.
[6] X. G. Yang, F. Y. Zhang, A. L. Lubawy, C. Y. Wang, Electrochem. Solid-State Letters 7 (11) (2004) A408-A411.
[7] T. Ochi, K. Kikuta, Y. Tabe, T. Chikahisa, Proc. 6th KSME-JASME Thermal and Fluid Engineering Conference (2005) [1/1 (CD-ROM) JJ-05] 1-4.
[8] Y. Tabe, T. Ochi, K. Kikuta, T. Chikahisa, H. Shinohara, Proc. 3rd Int. Conf. Fuel Cell Science, Engineering and Technology (2005) [1/1 (CD-ROM) 74172] 1-6.
[9] X. Zhu, P. C. Sui, N. Djilali, J. Power Sources 172 (2007) 287-295.
[10] P. K. Sinha, C. Y. Wang, Electrochim. Acta 52 (2007) 7936-7945.
[11] V. P. Schulz, J. Becker, A. Wiegmann, P. P. Mukherjee, C. Y. Wang, J. Electrochem. Soc. 154 (4) (2007) B419-B426.
[12] T. Inamuro, T. Ogata, S. Tajima, S. Konishi, J. Comput. Phys. 198 (2004) 628-644.
[13] S. Succi, The Lattice Boltzmann Equation for Fluid Dynamics and Beyond, Oxford Science Publications, New York, 2001.
[14] T. Seta, R. Takahashi, Proc. 14th Computational Engineering Conference 01-10 (2001) 541-542 (in Japanese).
[15] J. H. Ferziger, M. Perić, Computational Methods for Fluid Dynamics, Springer, Berlin, 1996.
[16] R. Lenormand, J. Phys. Condes. Matter 2 (1990) SA79.
[17] A. Kumar, R. G. Reddy, J. Power Sources 129 (2004) 62-67.
[18] S. Arisetty, A. K. Prasad, S. G. Advani, J. Power Sources 165 (2007) 49-57.
[19] S. Litster, D. Sinton, N. Djilali, J. Power Sources 154 (2006) 95-105.

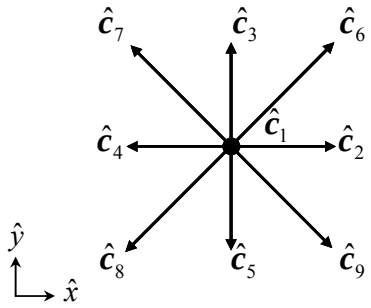
$\hat{\boldsymbol{c}}_7$
$\hat{\boldsymbol{c}}_3$
$\hat{\boldsymbol{c}}_6$
$\hat{\boldsymbol{c}}_1$
$\hat{\boldsymbol{c}}_4$
$\hat{\boldsymbol{c}}_2$
$\hat{\boldsymbol{c}}_8$
$\hat{\boldsymbol{c}}_5$
$\hat{\boldsymbol{c}}_9$
$\hat{y}$
$\hat{x}$

Fig. 1

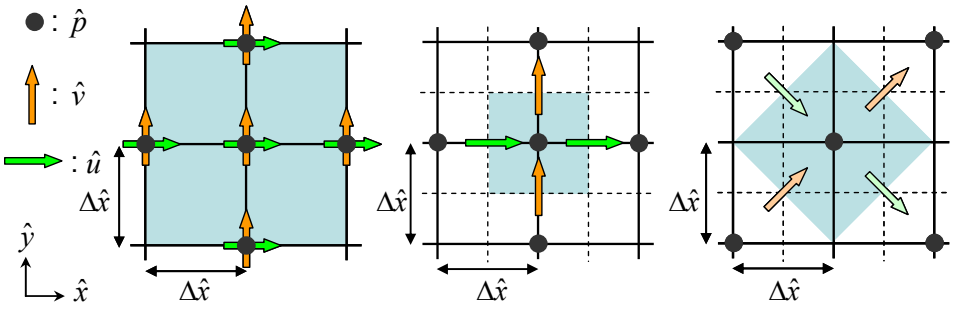

(a) Co-locate grid (b) Staggered grid 1 (c) Staggered grid 2

Fig. 2

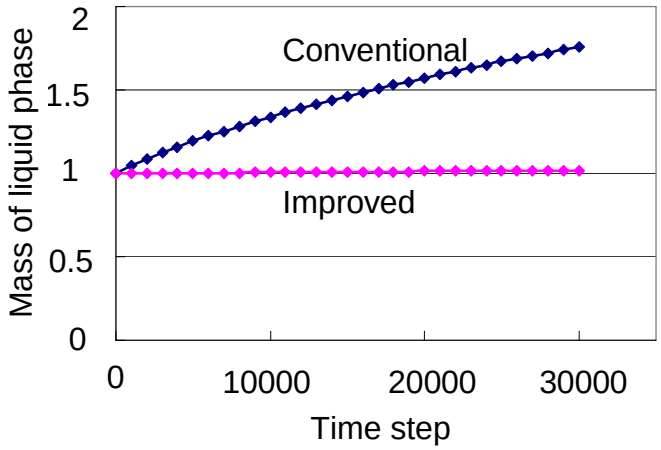
Mass of liquid phase
2
1.5
1
0.5
0
Conventional
Improved
0
10000
20000
30000
Time step

Fig. 3

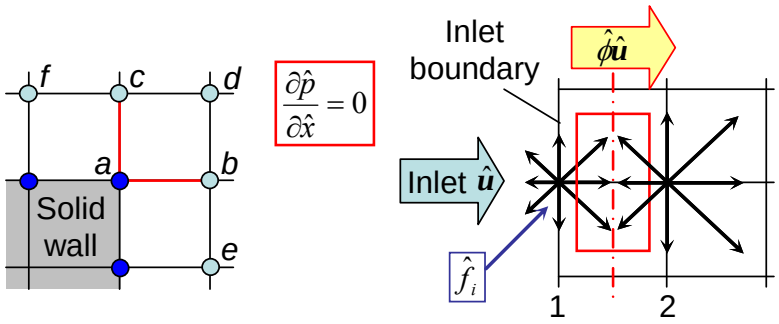

(a) Pressure $\hat{p}$ at the corner (b) Particle distribution function $\hat{f}_i$ at the inlet

Fig. 4

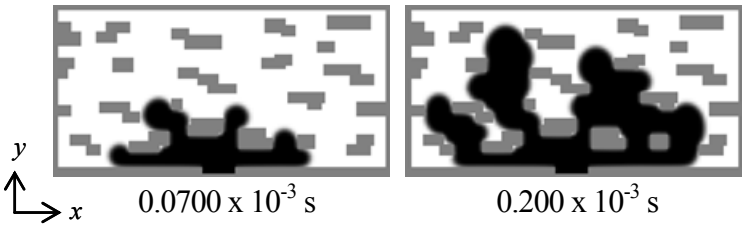

(a) $u_L^{in} = 2.0$ m s^{-1} ($Ca = 2.3$ x 10^{-2})

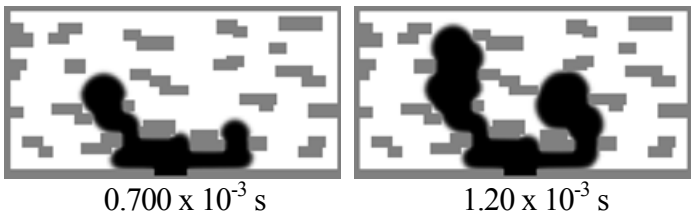

(b) $u_L^{in} = 0.20$ m s^{-1} ($Ca = 2.3$ x 10^{-3})

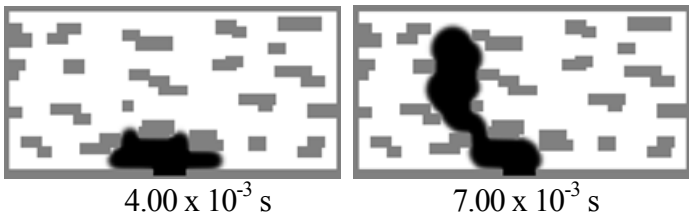

(c) $u_L^{in} = 0.020$ m s^{-1} ($Ca = 2.3$ x 10^{-4})

Fig. 5

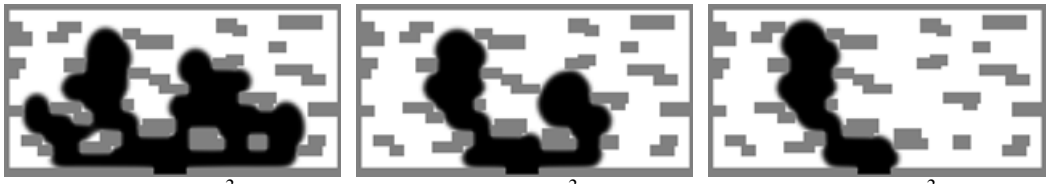

2.00×10^{-3} s | 12.0×10^{-3} s | 70.0×10^{-3} s

(a) $u_L^{in} = 2.0$ m s^{-1} ($Ca = 2.3 \times 10^{-2}$)

(b) $u_L^{in} = 0.20$ m s^{-1} ($Ca = 2.3 \times 10^{-3}$)

(c) $u_L^{in} = 0.020$ m s^{-1} ($Ca = 2.3 \times 10^{-4}$)

Fig. 6

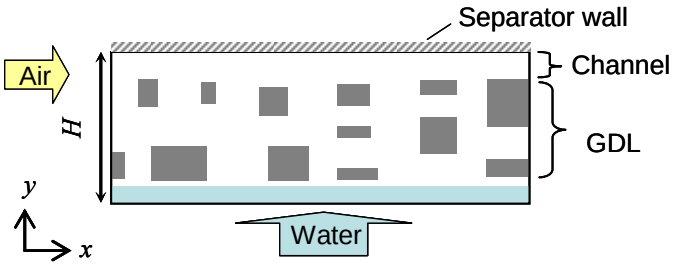

Fig. 7

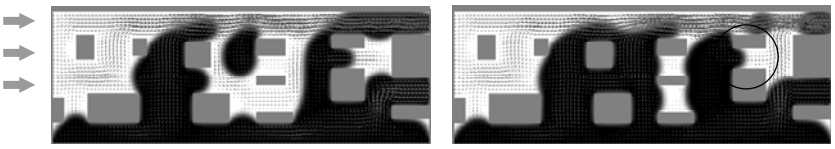

(a) 27.7×10^{-3} s (b) 44.9×10^{-3} s

Fig. 8

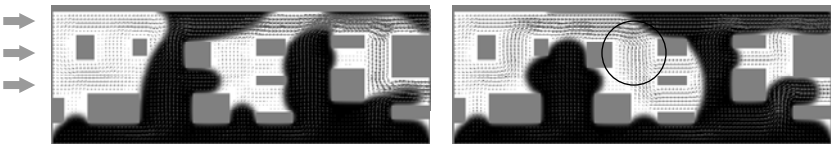

(a) 20.0 x 10^{-3} s (b) 35.8 x 10^{-3} s

Fig. 9

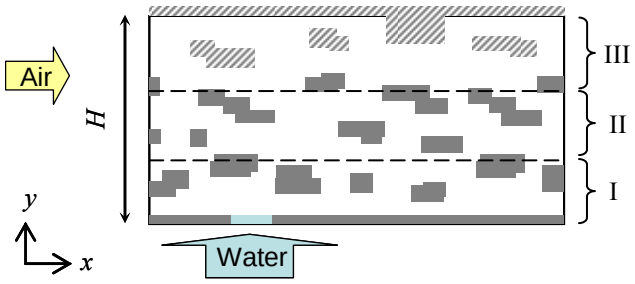

Fig. 10

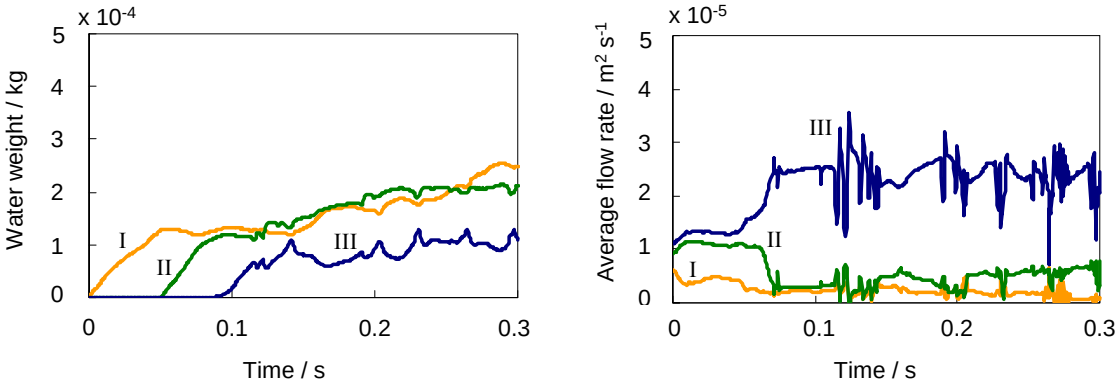

(a) Water weight

(b) Average air flow rate

Fig. 11

(a) 0.100 s (b) 0.150 s (c) 0.240 s

Fig. 12

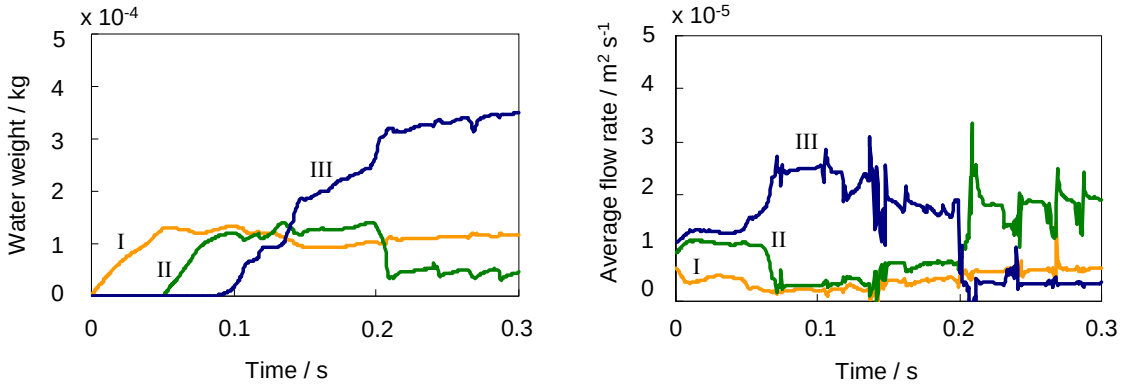

(a) Water weight

(b) Average air flow rate

Fig. 13

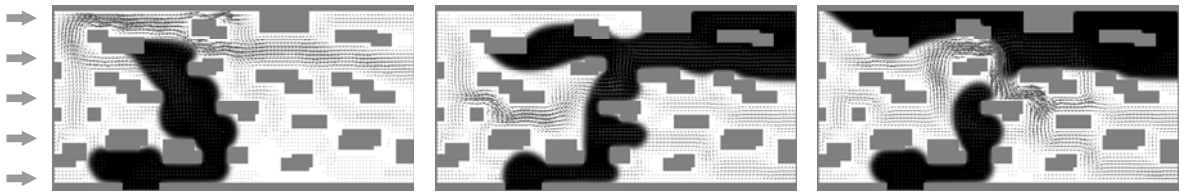

(a) 0.106 s (b) 0.207 s (c) 0.240 s

Fig. 14